Confocal energy-dispersive X-ray diffraction tomography employing a conical shell beam

A.J. Dicken,[1] J.P.O. Evans,[1,*] K.D. Rogers,[2] D. Prokopiou,[2] S.X. Godber,[3] F. Elarnaut,[1] A. Shevchuk,[1] D. Downes,[1] and M. Wilson[4]

[1]*Imaging Science Group, Rosalind Franklin Building, Nottingham Trent University, Nottingham, UK*
[2]*Cranfield Forensic Institute, Cranfield University, Shrivenham, Swindon, UK*
[3]*Halo X-ray Technologies, BioCity, Nottingham, UK*
[4]*STFC, Detector Development Group, Rutherford Appleton Laboratory, Didcot, UK*
*paul.evans@ntu.ac.uk

Abstract: We introduce a new high-energy X-ray diffraction tomography technique for volumetric materials characterization. In this method, a conical shell beam is raster scanned through the samples. A central aperture optically couples the diffracted flux from the samples onto a pixelated energy-resolving detector. Snapshot measurements taken during the scan enable the construction of depth-resolved dark-field section images. The calculation of d-spacing values enables the mapping of material phase in a volumetric image. We demonstrate our technique using five ~15 mm thick, axially separated samples placed within a polymer tray of the type used routinely in airport security stations. Our method has broad analytical utility due to scalability in both scan size and X-ray energy. Additional application areas include medical diagnostics, materials science, and process control.

1. Introduction

The high penetration power of X-rays is the basis for projection radiography and X-ray computed tomography. These modalities are highly developed and deployed routinely within security screening, industrial inspection, and medical diagnostics. Within this broad application space, there are many critical spatial imaging tasks, which would also benefit from the identification of material phase attributed to components within a volume. The spectroscopic analysis of transmitted X-rays can provide some useful materials discrimination information [1]. However, such methods are limited fundamentally, as the image forming X-rays incident on a detector have propagated along linear paths without interacting with the sample. Conversely, crystallography deals with the collection of coherently scattered or diffracted X-rays from a sample to enable structural analysis or 'molecular fingerprinting'. Traditional XRD instruments or diffractometers may be categorized into either angular [2] or energy dispersive [3–6] modalities. The former employs monochromatic radiation to measure the diffraction angle, *2θ*, subtended by the diffracted flux (from a sample) and the primary beam, while the latter measures the energy or wavelength, *λ*, at a fixed, known diffraction angle. Bragg's condition, $\lambda = 2d \sin \theta$, enables lattice parameters, e.g. d-spacings, to be calculated in each case. Laboratory scale instruments employ typically bright X-ray sources, e.g. 40 mA at ~40 kV. The amount of diffracted flux from a sample is relatively small and <<1% in comparison with the incident primary flux. Even with the use of a bright source and carefully prepared samples, the measurement time can range from minutes to hours.

Ultimately, the driver for our work is the detection and identification of homemade explosives (HMEs) and narcotics within the carry-on and checked luggage security at airports. A practical scanner requires exposure times of the order of seconds or less per measurement. There has been a considerable effort in developing high-energy methods utilizing novel X-ray beam topologies [2,3,7–12] and/or post-sample encoders [4,5,12–15]. Focal construct geometry (FCG) is an example of the former, which exploits the 'lensing' of

diffracted flux by extended gauge volumes produced by a conical shell beam of radiation incident on a sample. This technology is capable of providing depth-resolved material specific signatures without prior knowledge of the sample location [12]. We demonstrate an augmented version of this imaging architecture that produces a volumetric reconstruction of a heterogeneous phantom to validate our theoretical treatments.

The organization of our paper is as follows. Section 2 presents the methods and includes the theory background; our new tomographic approach and describes the experiment conditions. Section 3 presents our experiment results and discussion. Section 4 summarizes our conclusions, discusses the implications of our findings and the future direction of the work.

2. Methods

2.1 Theory background

FCG employs a conical shell X-ray beam to produce bright material specific patterns in the diffracted flux from samples. The extended annular gauge volumes provide a relative increase in the total number of crystallites of the correct orientation that satisfy Bragg's condition. The result is a significant increase in the diffracted intensity, resulting in reduced exposure times and/or a lower X-ray power burden. This beam topology has been implemented in energy [3] and angular dispersive modes [2,8–11], used to identify liquid samples [8] and shown to deal favorably with crystallographic textures [2,3,9,10] (i.e. preferred orientation and large grain size) that are known to be problematic [16,17]. Other implementations include the production of absorption tomography [18] and angular dispersive tomography [19] via raster scanning of annular projections over two orthogonal axes. Recently, we have demonstrated snapshot FCG [12] providing depth-resolved XRD patterns from a single stationary exposure. This paper describes a tomographic method in which a raster scanning snapshot FCG probe directly measures XRD sections to enable material specific volumetric visualizations.

2.2 New imaging technique

The FCG snapshot probe shown in Fig. 1 employs a post sample encoding-aperture optically coupled to a pixelated energy resolving detector. No prior positional information is required to provide depth-resolved XRD patterns. Diffracted rays propagate from within the shell beam's intersection with a sample (or gauge volume) onto a spatially resolving detection surface via a circular aperture. The linear distances x_D and y_D specify a position on the detection surface with respect to an origin defined by the piercing point of the shell beam symmetry axis, as shown in Fig. 1. The polar coordinates are given by

$$\alpha = \tan\left(\frac{y_D}{x_D}\right) \tag{1}$$

$$r = \frac{y_D}{\cos\alpha} = \frac{x_D}{\sin\alpha} \tag{2}$$

where α is the polar angle subtended at the center of the circular beam footprint and r is the polar radius. The separation between the detector and aperture is specified as a focal length f = D-A, as shown in Fig. 1. The diffraction angle 2θ is a function of the focal length f, the radius of the detected photon r and the half-opening angle of the conical shell beam ϕ as given by

$$2\theta = \tan^{-1}\left(\frac{r}{f}\right) + \phi. \tag{3}$$

Energy measurement at a detector pixel provides the wavelength λ of an incident photon via the Planck-Einstein relation. The associated d-spacing value may be calculated as a function of dependent variables r and λ by substituting for θ in Bragg's condition, to give

$$d = \frac{\lambda}{2\sin\left\{\dfrac{1}{2}\left[\tan^{-1}\left(\dfrac{r}{f}\right)+\phi\right]\right\}}. \qquad (4)$$
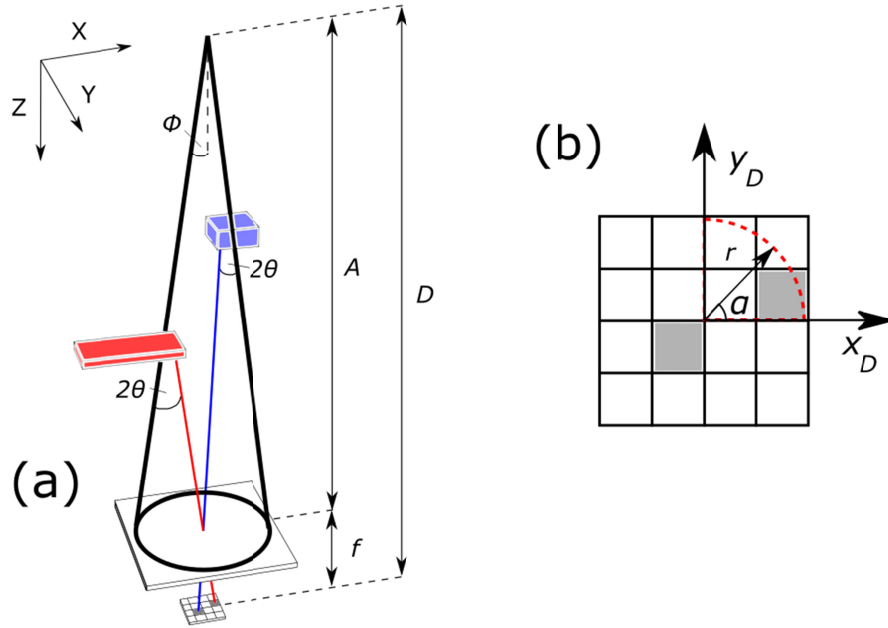

Fig. 1. (a) Coordinate system diagram illustrating a conical shell X-ray beam incident upon a pair of samples with unknown relative positions. The diffracted flux from the samples is collected via a central aperture onto a pixelated energy-resolving detector. (b) Polar coordinates r and α or Cartesian pixel distances y_D, x_D describe the local sample position and the diffraction angle. The beam, aperture and detector form a rigid body, which is raster scanned along axial directions x_t and y_t to collect and measure diffracted flux from samples distributed over the inspection volume.

Previous snapshot configurations [12] have only been concerned with encoding the local source-to-sample distance, which is given by

$$z_l = \frac{Ar}{r + f\tan\phi} \qquad (5)$$

where A is the source-to-aperture distance as shown in Fig. 1(a). The axial position (x_l, y_l) from which a photon is diffracted is given by

$$x_l = z_l \tan\phi\cos\alpha \qquad (6)$$

$$y_l = z_l \tan\phi\sin\alpha. \qquad (7)$$

The shell beam, encoding aperture and detector are raster scanned over the inspection volume. The relative offset x_t, y_t of the origin of the local coordinate system for each successive measurement or snapshot is discretized or scanned through axial step sizes Δx_t and Δy_t, respectively. The global coordinates of measured scattered photons are given by

$$x_g = x_l + x_t \qquad (8)$$

$$y_g = y_l + y_t \qquad (9)$$

$$z_g = z_l. \qquad (10)$$

The global Cartesian coordinate system (x_g, y_g, z_g) can describe the spatial distribution of coherent scatter measurements and or d-spacing information via Eq. (4) so enabling the construction of a volumetric data set.

2.3 Experiment conditions

Experiments were conducted using an IXS series VGA X-ray source operating at 160 kV accelerating voltage and 5 mA current. A conical shell beam was produced with the aid of a bespoke tungsten optic with a mean half-opening angle $\phi = 2.5°$ where $\phi_{max} = 2.55°$, $\phi_{min} = 2.45°$. A pinhole aperture of radius 0.75 mm in a 4 mm thick lead sheet, was placed 785 mm from the X-ray source. Scattered X-rays were detected using a 250 μm pitch (80^2 pixels) 20x20x1 mm³ cadmium telluride (CdTe) energy resolving detector placed at 895 mm from the X-ray source. The aperture-to-detector separation or focal length $f = 110$ mm is fixed throughout the experiments. The energy resolution of the detector ΔE at FWHM was estimated to be ~850 eV at 60 keV [20]. The phantom consisted of a polymer 'security' tray (see Fig. 2.) containing five ~15 mm thick, 90 mm diameter Petri dish samples (detailed in Table 1) positioned ~500 mm (z-axis) from the X-ray focus. The incident beam diameter is ~44 mm with a wall thickness of ~0.9 mm. The symmetry axis of the shell beam is orthogonal to the (x_g, y_g) plane. A two-axis raster scan comprises stepwise translation of the polymer tray along the x-axis with synchronized translation of the snapshot probe back and forth along the y-axis. In this way diffracted flux measurements from each detector pixel were integrated for 1 second over successive axial intervals of $\Delta y_t = 25$ mm. At the end of each (y-axis) linear scan the polymer tray was stepped by $\Delta x_t = 25$ mm before scanning the probe along the reverse (y-axis) direction. This sampling regime enabled the collection of 576 measurements/pixel over a total inspection area in the translation plane of ~600x600 mm².

Table 1. Details of the five samples used in the experiments.

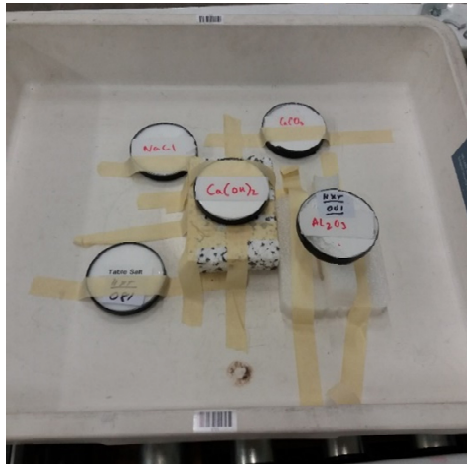| Material ID	Sample material	Thickness (mm)	Crystallographic texture	ICDD standard card number
a, b	Sodium chloride	15	Large grain size	00-001-0993
C	Calcite	15	Near NIST standard	00-005-0586
D	Calcium hydroxide	15	Near NIST standard	00-004-0733
E	Aluminum oxide	15	Near NIST standard	01-070-5679

Fig. 2. The heterogeneous 3D phantom consisted of a polymer tray containing five ~15mm thick, 90 mm diameter Petri dish samples with different crystallographic textures. The center sample and the bottom right sample are offset along the z-axis (i.e. distance from the source).

3. Results and discussion

Diffracted photons from the phantom were collected during a two-axis raster scan at local coordinates (x_l, y_l, z_l) as described by Eqs. (5)-(7). The measurements obtained from each detector element are at known multiples of $\Delta x_t = \Delta y_t = 25$ mm from a global scan origin. This snapshot pitch was sufficient to resolve the 90 mm diameter samples distributed over a 600 mm square inspection footprint. Thus, traversing the entire inspection volume facilitates the production of a 3D map of coherent scatter according to the global coordinates (x_g, y_g, z_g), as given by Eqs. (8)-(10) and presented as a volumetric image (and video) in Fig. 3. The intensity of each voxel is proportional to the sampled coherent scattering photon count across all measured energies.
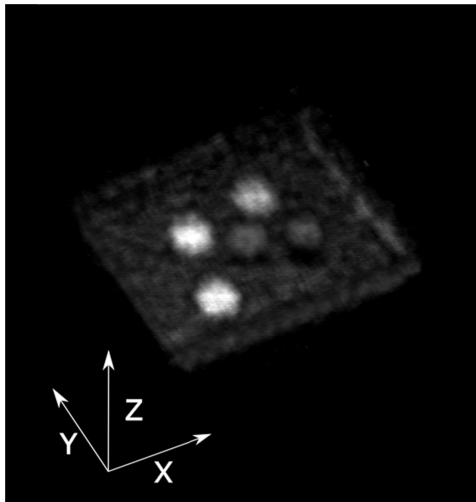

Fig. 3. Volumetric image (photograph shown in Fig. 2) from the integrated measurements of coherent X-ray scatter across all energy bands from five ~15mm thick, 90 mm diameter Petri dish samples placed on a polymer tray. A rotating image of the whole phantom, including the outline of the tray, can be seen in (Visualization 1).

In addition to the volumetric construction and visualization from the simple sum of coherent scatter, the measurement of diffracted flux from each gauge volume enables material

information to be calculated. The centrally positioned pinhole or encoding aperture enables the angle of diffraction 2θ given by Eq. (3) to be calculated. Thus, material specific scattering distributions can be calculated for each voxel. Conventional 1D diffractograms for the five samples (listed in Table 1) are presented in Fig. 4(a) and were created by integrating the signals in the corresponding regions of interest highlighted in Fig. 4(b). Peak positions from reference patterns obtained from the ICDD PDF4 database are also presented in Fig. 4(a). Integrating the spectral flux measurements from an extended gauge volume increases the total number of crystallites providing enhanced particle statistics. This method increased the repeatability of measurements in the presence of crystallographic texture effects such as large grain size, these have been shown to be problematic in competing EDXRD techniques [16,17]. An example of repeatability in measurement in the presence of texture is illustrated by the good agreement between the diffractograms of materials '*a*' and '*b*' (i.e. large grain size sodium chloride) shown in Fig. 4(a) and further supports our previous EDXRD experimental findings presented elsewhere [3,12]. In practice, the requirement for a finite aperture size and the angular spread of the primary beam $\Delta\phi$, about a mean angle ϕ, produce an error in the 2θ measurement of $\Delta 2\theta$, which together with the energy resolution of the detector ΔE determine the precision of the d-spacing. We calculate a d-spacing error (Δd, $\mathring{A}$) for the 1.99 Å (220) plane in sodium chloride to be $\pm \sim 0.2$ Å, which appears consistent with our diffractograms as illustrated in Fig. 4(a); the derivation of this analysis has been described and explored elsewhere [12].
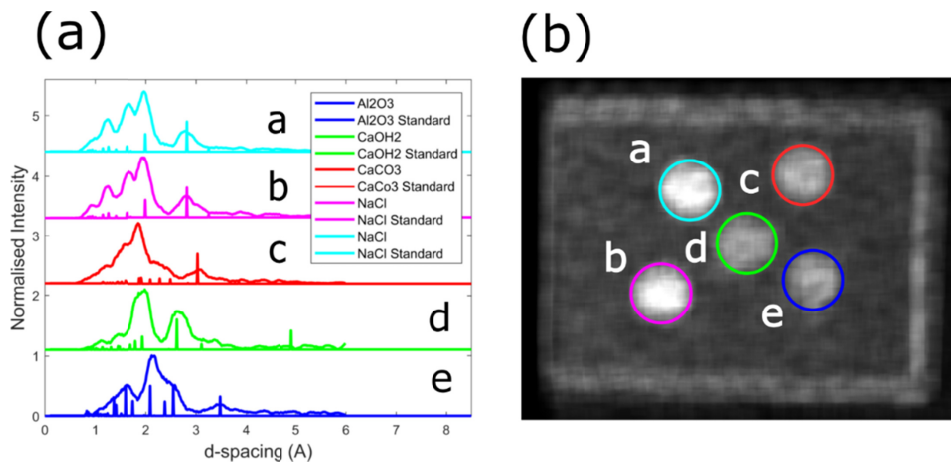

Fig. 4. (a) Conventional 1D-diffractograms for the five samples detailed in Table 1. These are generated by integrating the signals in the corresponding regions of interest as highlighted in the coherent scattering z projection (b).

To estimate the spatial fidelity of the reconstructed image parameters we model the envelop of the diffracted flux (Eq. (1) [12]) from the NaCl samples, labelled a and b in Fig. 4(b), located at a mean distance of ~512 mm (520 mm - 505 mm) from the X-ray focus. Our analysis predicted a reconstructed thickness of ~37 mm (493 mm - 530 mm), which agreed well with observations of the experiment results. This effect was mainly attributed to the finite diameter of the encoding aperture and the angular range of the shell beam. It also indicates that the z-axis spatial resolution is nominally independent of the transverse axial step sizes Δx_t and Δy_t. This finding was expected as the beam and detector translate together during the raster scan as a rigid body, which therefore means that the z-axis spatial resolution and d-spacing resolution are both determined by the local parameters and detector coordinates. The transverse spatial resolution was observed to be of the order of the axial step size (i.e. 25 mm) for optical sections ~512 mm along the z-axis.

4. Conclusions and future work

We have demonstrated coherent scattering tomography by raster scanning a conical shell beam through five spatially distributed samples contained on a polymer inspection tray. Measuring the angle of incidence and the energy of the diffracted photons from the samples, via a pinhole aperture optically coupled to a pixelated energy-resolving detector, enabled the calculation of material phase. Successive, depth-resolved snapshot exposures of 1 second enabled the *(x,y,z)* coordinate positions of the diffracted photons to be calculated and a volumetric image to be presented. Prior knowledge of sample position(s) was not required to calculate material specific lattice spacing information or d-spacing values in our experiment. Our imaging architecture can be setup to provide much greater spatial detail by reducing the snapshot pitch. By hypothesis, we anticipate the staring mode resolution [12] of the probe will limit spatial resolving power.

We believe our approach is potentially beneficial for fields including medicine and industrial process control. However, its application to checkpoint security scenarios is of immediate relevancy where ongoing work is optimizing our method for speed of operation. The materials information provided by our probe is orthogonal to the conventional Z-effective and density data provided by dual-energy computed tomography, as employed in checkpoint screening systems. Combining our XRD tomographic probe with dual-energy CT will provide new opportunities to further improve probability of detection and reduce false alarms in the presence of stream-of-commerce clutter.

Funding

References

1. K. Wells and D. A. Bradley, "A review of X-ray explosives detection techniques for checked baggage," Appl. Radiat. Isot. **70**(8), 1729–1746 (2012).
2. A. Dicken, A. Shevchuk, K. Rogers, S. Godber, and P. Evans, "High energy transmission annular beam X-ray diffraction," Opt. Express **23**(5), 6304–6312 (2015).
3. A. J. Dicken, J. P. O. Evans, K. D. Rogers, C. Greenwood, S. X. Godber, D. Prokopiou, N. Stone, J. G. Clement, I. Lyburn, R. M. Martin, and P. Zioupos, "Energy-dispersive X-ray diffraction using an annular beam," Opt. Express **23**(10), 13443–13454 (2015).
4. O. Lazzari, S. Jacques, T. Sochi, and P. Barnes, "Reconstructive colour X-ray diffraction imaging--a novel TEDDI imaging method," Analyst (Lond.) **134**(9), 1802–1807 (2009).
5. A. M. Beale, S. D. M. Jacques, E. K. Gibson, and M. M. Michiel, "Progress towards five dimensional diffraction imaging of functional materials under process conditions," Coord. Chem. Rev. **277–278**, 208–223 (2014).
6. E. J. Cook, J. A. Griffiths, M. Koutalonis, C. Gent, S. Pani, J. A. Horrocks, L. George, S. Hardwick, and R. Speller, "Illicit drug detection using energy dispersive X-ray diffraction," Proc. SPIE **7310**, 73100I (2009).
7. K. Rogers and P. Evans, "X-Ray Diffraction and Focal Construct Technology," in X-Ray Diffraction Imaging Technology and Applications, J. Greenberg, ed. (CRC, 2018).
8. D. Prokopiou, K. Rogers, P. Evans, S. Godber, and A. Dicken, "Discrimination of liquids by focal construct technology," Appl. Radiat. Isot. **77**, 160–165 (2013).
9. K. Rogers, P. Evans, J. Rogers, J. Chan, and A. Dicken, "Focal construct geometry – a novel approach to the acquisition of diffraction data," J. Appl. Cryst. **43**(2), 264–268 (2010).
10. P. Evans, K. Rogers, J. Chan, J. Rogers, and A. Dicken, "High intensity x-ray diffraction in transmission mode employing an analog of Poisson's spot," Appl. Phys. Lett. **97**(20), 1–3 (2010).
11. D. Prokopiou, K. L. Smith, K. Rogers, P. Paula, P. Evans, A. Dicken, and S. Godber, "Simulations and experimental demonstrations of encoding for X-ray coherent scatter," J. Appl. Cryst. **50**(2), 411–418 (2017).
12. A. J. Dicken, J. P. O. Evans, K. D. Rogers, D. Prokopiou, S. X. Godber, and M. Wilson, "Depth resolved snapshot energy-dispersive X-ray diffraction using a conical shell beam," Opt. Express **25**(18), 21321–21328 (2017).
13. D. O'Flynn, C. Crews, I. Drakos, C. Christodoulou, M. D. Wilson, M. C. Veale, P. Seller, and R. D. Speller, "Materials identification using a small-scale pixelated x-ray diffraction system," J. Phys. D Appl. Phys. **49**(17), 175304 (2016).

14. M. Hassan, J. A. Greenberg, I. Odinaka, and D. J. Brady, "Snapshot fan beam coded aperture coherent scatter tomography," Opt. Express **24**(16), 18277–18289 (2016).
15. Z. Zhu, A. Katsevich, A. J. Kapadia, J. A. Greenberg, and S. Pang, "X-ray diffraction tomography with limited projection information," Sci. Rep. **8**(1), 522 (2018).
16. B. Ghammraoui, V. Rebuffel, J. Tabary, C. Paulus, L. Verger, and P. Duvauchelle, "Effect of grain size on stability of X-ray diffraction patterns used for threat detection," Nucl. Instrum. Methods Phys. Res. A **683**, 1–7 (2012).
17. J. A. Greenberg, C. MacGibbon, D. Hazineh, B. Keohane and S. Wolter, "The role of texturing in x-ray diffraction tomography," Proc. of Spie **10632**, 106320B1–9 (2018).
18. J. P. O. Evans, S. X. Godber, F. Elarnaut, D. Downes, A. J. Dicken, and K. D. Rogers, "X-ray absorption tomography employing a conical shell beam," Opt. Express **24**(25), 29048–29059 (2016).
19. P. Evans, K. Rogers, A. Dicken, S. Godber, and D. Prokopiou, "X-ray diffraction tomography employing an annular beam," Opt. Express **22**(10), 11930–11944 (2014).
20. P. Seller, S. Bell, R. J. Cernik, C. Christodoulou, C. K. Egan, J. A. Gaskin, S. Jacques, S. Pani, B. D. Ramsey, C. Reid, P. J. Sellin, J. W. Scuffham, R. D. Speller, M. D. Wilson, and M. C. Veale, "Pixellated Cd(Zn)Te high-energy X-ray instrument," J. Instrum. **6**(12), C12009 (2011).